ORIGINAL PAPER

The hemodynamics in intracranial aneurysm ruptured region with active contrast leakage during computed tomography angiography

**Ming-Lung Li · Yi-Chou Wang ·
Tong-Miin Liou · Chao-An Lin**

Abstract Precise locations of rupture region under contrast agent leakage of five ruptured cerebral artery aneurysms during computed tomography angiography, which is to our knowledge for the first time, were successfully identified among 101 patients. These, together with numerical simulations based on the reconstructed aneurysmal models, were used to analyze hemodynamic parameters of aneurysms under different cardiac cyclic flow rates. For side wall type aneurysms, different inlet flow rates have mild influences on the shear stresses distributions. On the other hand, for branch type aneurysms, the predicted wall shear stress (WSS) correlates strongly with the increase of inlet vessel velocity. The mean and time averaged WSSes at rupture regions are found to be lower than those over the surface of the aneurysms. Also, the levels of the oscillatory shear index (OSI) are higher than the reported threshold value, supporting the assertion that high OSI correlates with rupture of the aneurysm. However, the present results also indicate that OSI level at the rupture region is relatively lower.

Keywords Intracranial aneurysm · Hemodynamic ·
Rupture point · Wall shear stress

M.-L. Li
National Center for High-Performance Computing,
Hsinchu 300, Taiwan

Y.-C. Wang
Chang Gung University and Chang Gung Memorial Hospital,
Taoyuan, Taiwan

M.-L. Li · T.-M. Liou · C.-A. Lin (✉)
Department of Power Mechanical Engineering,
National Tsing Hua University, Hsinchu 30013, Taiwan
e-mail: calin@pme.nthu.edu.tw

1 Introduction

Intracranial aneurysms pose a major threat to a patient's life, because of the disastrous complications that can arise if they rupture. Accurate criteria for predicting aneurysm rupture are important for therapeutic decision-making, and some clinical and morphological factors may help to predict the risk for rupture of unruptured aneurysms, such as sex, size and location [1–4].

Hemodynamic factors and morphology parameters are considered to be among the primary contributors to aneurysm rupture [5]. Dhar et al. [6] and Ma et al. [7] identified image-based morphological parameters that correlate with human intracranial aneurysm rupture Hemodynamic factors and morphology parameters are considered to be among the primary contributors to aneurysm rupture [5]. Dhar et al. [6] and Ma et al. [7] identified image-based morphological parameters that correlate with human intracranial aneurysm rupture, such as aspect ratio (AR), non-sphericity index (NSI) and undulation index (UI).

Based on 3D imaging and simulation technology, patient-specific hemodynamics analysis has become feasible [8–11]. The aneurysmal hemodynamic factors, such as wall shear stress (WSS) and oscillatory shear index (OSI), have been proposed as indicators of aneurysm rupture risk [12, 13]. However, opposing hypotheses have shown that high [12] or low [13] WSS is responsible for aneurysm rupture. Shojima et al. [14] have demonstrated that maximal WSS tends to occur near the neck of an aneurysm, rather than in the tip or bleb, and that the average WSS for an aneurysm region is significantly lower than that for the vessel region. Additionally, Jou et al. [15] found that ruptured aneurysms had a greater portion of their surface under low WSS than unruptured aneurysms (27 vs. 11 %).

It should be noted that rigid wall was adopted in most previous studies. However, development of numerical algorithm [16,17] allows the simulations of the fluid and structure interaction within the cerebral aneurysms [18–23] and explores its influence on the aneurysm hemodynamic factors. For example, Valencia [18] showed that the predicted maximum WSS with elastic wall could be 50 % lower than its rigid wall counterpart. Also, Torii et al. [19] indicated that the reduction was particularly evident in impingement type flow. Strategy as how to enhance the calculations of WSS and OSI was addressed by Takizawa et al. [20]. Torii et al. [22] further examined the influencing factors during FSI on the WSS distribution and the impact of the arterial and aneurysm geometries was deemed to be most significant. A review of fluid-structure modeling of patient specific cerebral aneurysm can be found in [24].

On the other hand, localizing the rupture point is essential in studies investigating the hemodynamic forces potentially responsible for the rupture of aneurysms. However, the rupture point could not be accurately identified in previous studies, which were reliant upon indirect observations. Some have suggested that small blebs or daughter sacs are points of rupture, while others have identified the rupture point from observations of the aneurysm during operations. Neither of these methods can accurately localize the true point of rupture. In [25], it was showed that the rupture point is located in a low WSS region of the aneurysm wall. However, the determination of the rupture point was not obtained from contrast agent leakage identified from the computed tomography angiography (CTA) images.

Based on the above, there are two goals of the present study. The first one is to detect the location of the aneurysm rupture from the patient's CTA images during contrast agent leakage. Up to now, to our knowledge, there is no reported study in identifying the location of the aneurysm rupture through CTA images at contrast agent leakage. The second goal is to clarify the association between aneurysm rupture points and hemodynamic features, such as WSS and OSI through numerical simulations of the dyanmic fields within the aneurysms. Since now the location of the aneurysm rupture can be identified from CTA images, it is hope that the present study could help to clarify whether high or low WSS promotes the rupture of aneurysms and confirm the previously proposed morphological parameters [6] in diagnosing aneurysm rupture risk.

2 Materials and Methods

2.1 Subject

This study included 5 patients, 2 females and 3 male aged between 53 and 80 years, with ruptured middle cerebral artery aneurysms treated by neck clipping from among 101 patients. Contrast extravasation during CTA was observed in 5 of these patients. 3D CTA was performed in all patients. Only 3D images of sufficient quality for accurate segmentation and reconstruction were included. The study protocol was approved by the local ethics committee.

2.2 Imaging

CT scanning was performed with a multisection spiral CT scanner (Somatom Sensation 16; Siemens Medical Solution, Forchheim, Germany). A power injector was used to inject 100 ml of nonionic iodinated contrast material (Omnipaque 350; GE Healthcare Ireland, Cork, Ireland) at a flow rate of 3.5 mL/s. The scanner's integrated bolus tracking method was used for bolus timing. The spiral scan was initiated when a 100 HU threshold was reached within the region of interest. A collimation of 16×0.75 mm with a table feed of 18 mm was used for the spiral scan, which covered the area from the aorta to the vertex of the skull. The image reconstruction was performed with a section thickness of 0.75 mm, an increment of 0.7 mm, and a 180-mm^2 field of view. Thus, both the circle of Willis and posterior inferior cerebellar arteries were completely included within the column. The resulting voxel size was $0.35 \times 0.35 \times 0.7$ mm^3.

2.3 Image reconstruction and processing

Digital images were transferred to a Macintosh workstation, and 3D vessels were reconstructed with the volume-rendering algorithm of open-source software OsiriX. The contrast leakage in each of the 5 patients could be seen as a string connecting to the aneurysm shown in Fig. 1. The skull, calcification of vessel wall, and soft tissue in the source CTA image were removed manually. Surface irregularities resulting from partial volume effects, truncated small arteries as well as other noise were also corrected manually using Amira (TGS, Inc., San Diego, CA). Table 1 displays the geometric details of the aneurysms.

2.4 Rupture points

No previous study reported the location and consequently the area of the ruptured point during contrast agent leakage. In this study, the precise point of contrast agent leakage was successfully identified from the CTA images, as shown in Fig. 1. However, the area of the rupture point is still not determined. Here, this is estimated to be 1–5% of the aneurysm surface and the corresponding surface areas are shown in Table 2. Figure 2 shows the rupture area based on this criterion. Sensitivity study on the predicted hemodynamic quantities is conducted in the latter section to explore its influence.

Fig. 1 Images of aneurysms from CTA during contrast agent leakage for cases A and B
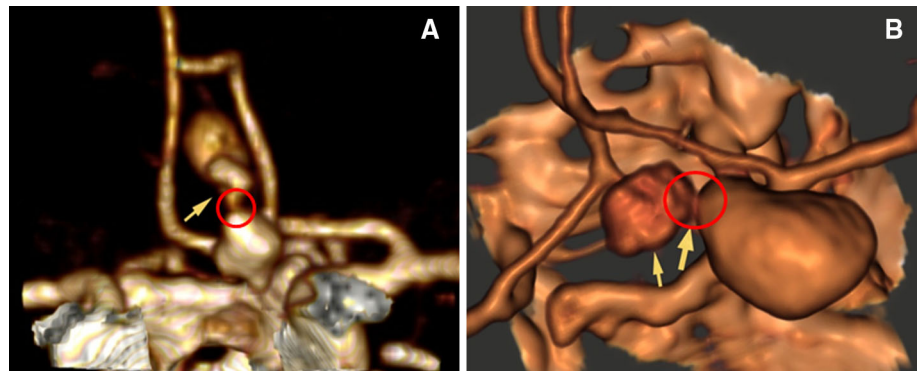
Table 1 Geometrical properties for all patients

Case	Size (mm)	Volume (mm³)	Surface (mm²)	Location
A	9.1	187.3	154	ACOM
B	16.5	1009.3	580	PCOM
C	13.8	437.4	231	BA
D	4.5	44.6	64	PCOM
E	7.9	139.8	119	MCA

ACOM anterior communicating artery, *PCOM* posterior communicating artery, *BA* basilar artery, *MCA* middle cerebral artery

Table 2 Ruptured area of 5, 2.5 and 1 % aneurysm surface for all patients

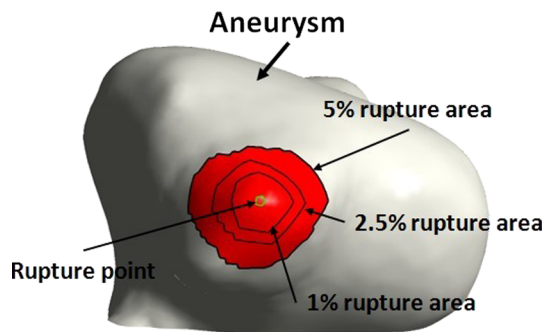| Case	5 % area (mm²)	2.5 % area (mm²)	1 % area (mm²)
A	7.70	3.85	1.54
B	29.0	14.5	5.80
C	11.6	5.80	2.31
D	3.20	1.60	0.64
E	5.95	2.96	1.19

Fig. 2 Rupture point area of aneurysm

2.5 Shape indices

Here, the morphological parameters explored, namely the AR, non-spherical index, and UI, are introduced, where the latter two are functions of the aneurysm volume (V), surface area (S) and its convex hull [7]. The convex hull volume (V_{ch}) is defined as the mimimum volume surrounding the aneurysm with convex hull surface (S_{ch}). The volume and surface area of the convex hull for each aneurysm studied are computed using the Convex Hull calculator in ANSYS ICEMCFD (ANSYS, Berkeley, CA).

AR is the ratio of the maximum perpendicular height to the average neck diameter. The NSI is defined as,

$$NSI = 1 - (18\pi)^{1/3} \frac{V^{2/3}}{S} \tag{1}$$

where V and S are as defined earlier, the volume and surface area of the aneurysm, respectively. NSI increases as the geometry of aneurysm deviating from the spherical shape.

The UI is defined as,

$$UI = 1 - \frac{V}{V_{ch}} \tag{2}$$

UI characterizes undulation of the aneurysm wall.

3 Numerical solution

3.1 Volumetric mesh generation

Computational grids based on five reconstructed aneurysm models were generated using ICEMCFD software (ANSYS, Berkeley, CA). The grids consist of 60,545–2,041,093 tetrahedral elements with 0.3-mm maximum element size in the aneurysm. Figure 3 shows the built grids and Table 1 displays the geometric details of the aneurysms. Solid lines on the aneurysm surfaces are the 5% rupture surface area.

Figure 4 shows the meshes at the inflow plane, showing respectively four and five structured refined meshes near the wall. Table 3 depicts the predicted mean WSS distribution within the aneurysm with zero, one, two, three, four and five layers of refined fluid mechanics mesh near the walls. The mesh resolution does influence computed WSS values, as

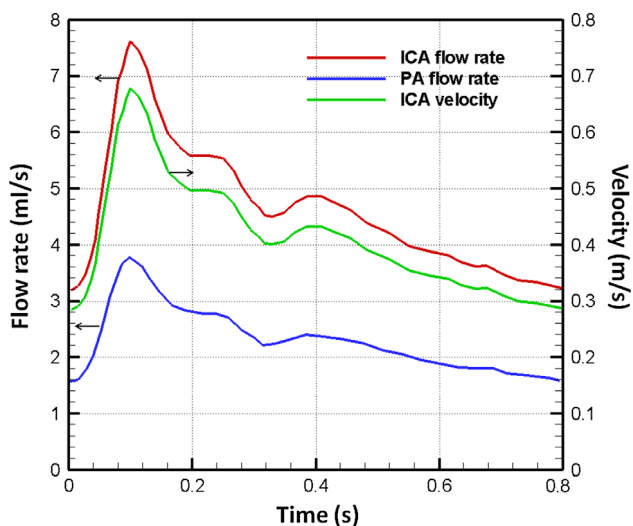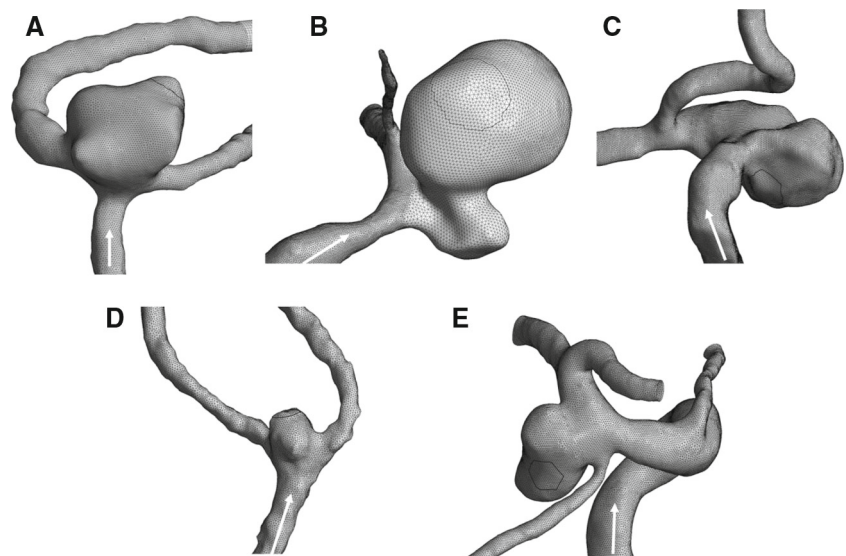**Fig. 3** Computational mesh of intracranial aneurysms

Fig. 4 Cardiac cyclic inlet conditions for simulations

Table 3 The WSS values calculated for refined fluid mechanics mesh near the arterial walls

Case	MWSS on aneurysm (Pa)
0 layer	3.80
1 layer	3.22
2 layers	3.35
3 layers	3.38
4 layers	3.40
5 layers	3.40

$$\frac{\partial \rho u_i}{\partial x_i} = 0 \tag{3}$$

$$\frac{\partial \rho u_i}{\partial t} + \frac{\partial \rho u_i u_j}{\partial x_j} = -\frac{\partial P}{\partial x_i} + \mu \frac{\partial u_i^2}{\partial x_j^2} \tag{4}$$

where u_i is the velocity, ρ is the fluid density, P the pressure, and μ is the fluid viscosity. The 3D unsteady Navier-Stokes equations were solved by using the finite control volume software, ANSYS-CFX 14.0 (ANSYS, Berkeley, CA). The second-order upwinding advection scheme was used. The time advancement is based on the implicit scheme and the algebraic multigrid method is adopted to solve for the linear equations. As mentioned earlier, blood was modeled as an incompressible Newtonian fluid with a density of 1,050 kg/m³ and a viscosity of 3.5×10^{-3} kg/m s. The minimum time-step was 0.01 s (for a 0.8 s cycle). The given boundary conditions were the no-slip and rigid condition on the wall, and zero pressure at the outlet.

Two cardiac cyclic volumetric flow rates respectively from posterior artery [27] and internal carotid artery [28] and one cyclic velocity profile were used as inlet conditions for the simulations, as shown in Fig. 5. The cyclic velocity profile
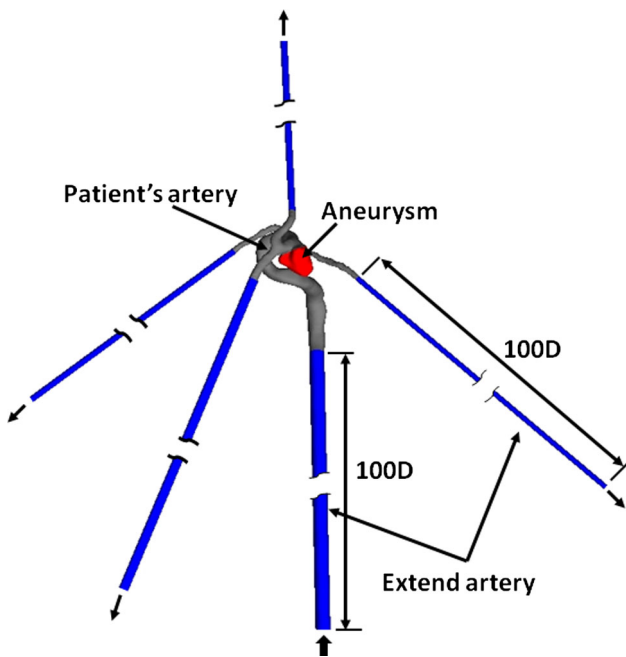
shown in Table 3. However, the predicted WSS value saturates beyond four layers of near wall mesh. Thus, in the present study, five layers of refined mesh near the wall region are adopted.

3.2 Hemodynamic models

In the present simulations, it is assumed that blood is an incompressible, Newtonian fluid and that the flow is laminar and isothermal. The assumption of Newtonian behavior is based on the findings of Perktold et al. [26] and others who found minimal changes in arterial flow patterns when non-Newtonian effects were included. For such a fluid, the continuity and Navier-Stokes equations are as follows:
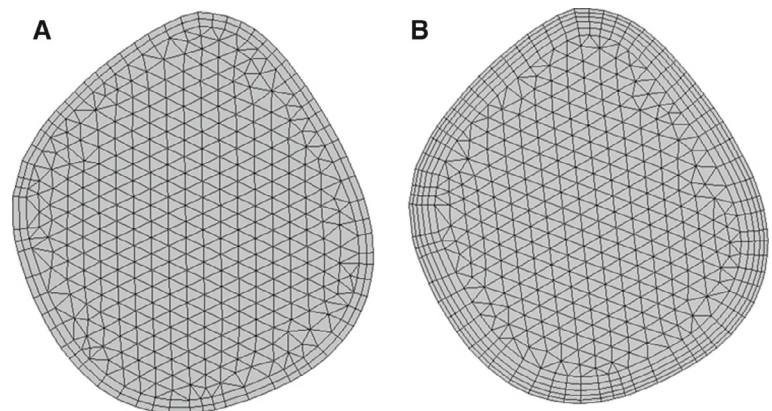
Fig. 5 Computational model of intracranial aneurysms

Table 4 Calculated morphological parameters

Case	AR	UI	NSI
A	2	0.09	0.24
B	4	0.23	0.65
C	2.3	0.15	0.24
D	3.7	0.08	0.32
E	1.4	0.18	0.14
Threshold [6]	1.4	0.05	0.16

is the inlet velocity of case B determined form the internal carotid artery volume flow rate. Since the inlet cross-section varies, the same flow rate would generate different inlet velocity. Thus, velocity inlet would provide indication as how this boundary conditions affect the results. WSS-based scaling technique for specifying more realistic volumetric flow rate at the inflow boundary was introduced recently by Takizawa and Tezduyar [24]. This technique is worth investigated in future study.

In general, the inlet section is not circular. A special mapping technique was proposed by Takizawa et al. [21] to specify the velocity profile at an inflow boundary for a non-circular shape artery. In the present study, the inlet and outlet are placed at least 100 artery diameters upstream and downstream of the aneurysm, as shown in Fig. 6. This allows

the inlet profile to become fully developed before it reaches the aneurysm and prevents the downstream influence on the internal flow. Also, the cutting planes at the artery inlets and outlets are perpendicular to the flow direction, as shown Fig. 6.

Unsteady simulations were initialized from a steady-state solution based on end diastolic flow rates. No data were analyzed until after the five cardiac cycles, since it was determined by computational experiment that five cycles were sufficient to nullify the transient artefact generated by the initial conditions. All simulations were run in parallel on AMD Opteron 6174 2.2 GHz 64-bit 8 core processors on Acer AR585 F1 Cluster. The average time required to solve five cardiac cycle with the meshes considered was approximately 10 hour.

3.3 Hemodynamic parameter

Two hemodynamic parameters were investigated here, i.e. time averaged wall shear stress (TAWSS) and OSI, which can be calculated from the simulated flow fields. The TAWSS for pulsatile flow was calculated by integrating the WSS at each node over the cardiac cycle [29]:

$$TAWSS = \frac{1}{T} \int_0^T |\tau| dt \tag{5}$$

Fig. 6 Mesh at the inflow plane for two layers and five layers near the wall

Table 5 Mean wall shear stress (MWSS) at the rupture point and aneurysm wall with Posterior Artery flow rate

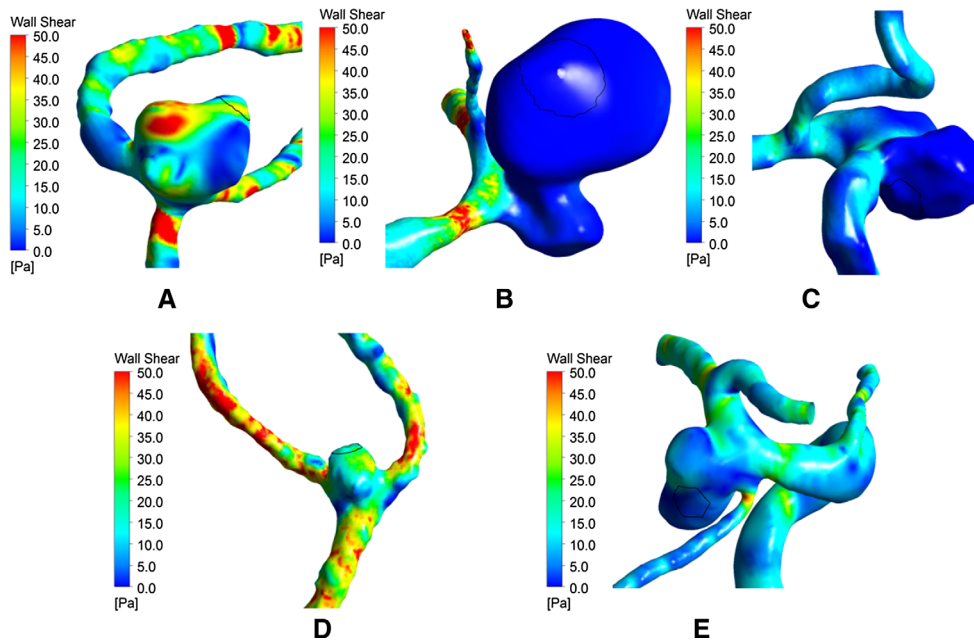| Case	Aneurysm wall (Pa)	Ruptured point (Pa)			Ruptured/aneurysm (%)		
		5 %	2.5 %	1 %	5 %	2.5 %	1 %
Peak systole (t = 3.3 s)							
A	18.11	17.79	17.73	13.94	98	98	77
B	0.88	0.07	0.06	0.05	7	7	6
C	1.97	0.31	0.24	0.20	16	12	10
D	75.35	24.93	17.90	18.05	33	24	24
E	8.95	3.43	2.84	2.76	38	32	31
End diastole (t = 4 s)							
A	5.20	4.96	4.91	3.93	95	94	76
B	0.34	0.03	0.03	0.02	9	8	7
C	0.70	0.17	0.13	0.10	25	19	15
D	16.05	6.12	6.00	6.52	38	37	41
E	2.43	1.23	1.10	1.09	50	45	45

Fig. 7 Mean WSS on aneurysm at peak systole phase with posterior artery flow rate

where τ is the instantaneous shear stress vector and T is the duration of the cycle. WSS is obtained from the ANSYS built function. OSI, a nondimensional parameter, measures the directional change of WSS during the cardiac cycle [14]:

$$OSI = \frac{1}{2}\left[1 - \frac{\left|\int_0^T \tau\, dt\right|}{\int_0^T |\tau|\, dt}\right] \qquad (6)$$

OSI is often used to describe the disturbance of a flow field.

4 Results and discussion

As was indicated previously, morphological parameters, such as AR, UI, and NSI can be used to diagnose the possibility of aneurysm rupture risk. It is thus beneficial here to examine the current values of the examined cases against the optimal thresholds of aneurysm rupture, i.e. AR = 1.4, NSI = 0.16, UI = 0.05 reported in [6]. By reference to Table 4, the current values of AR, UI and NSI are respectively between 1.4 and 4.0, 0.08 and 0.23 and 0.14 and 0.65, which are significantly higher than the reported optimal thresholds. Since the present cohorts are rupture aneurysms, so the results are not surprising.
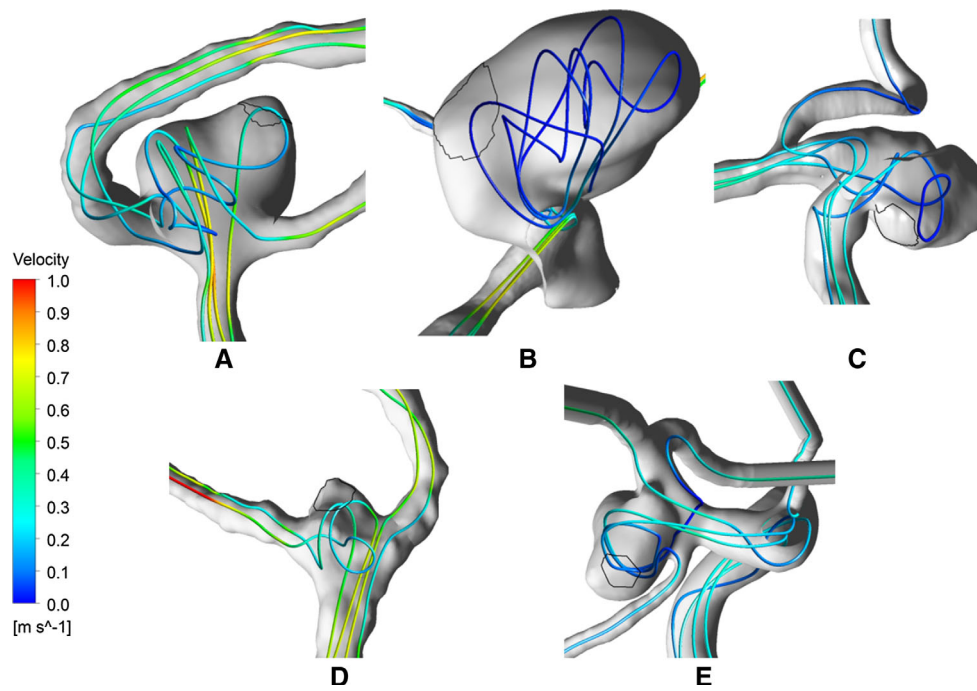
Fig. 8 Streamline distributions of intracranial aneurysm at peak systole phase with posterior artery flow rate
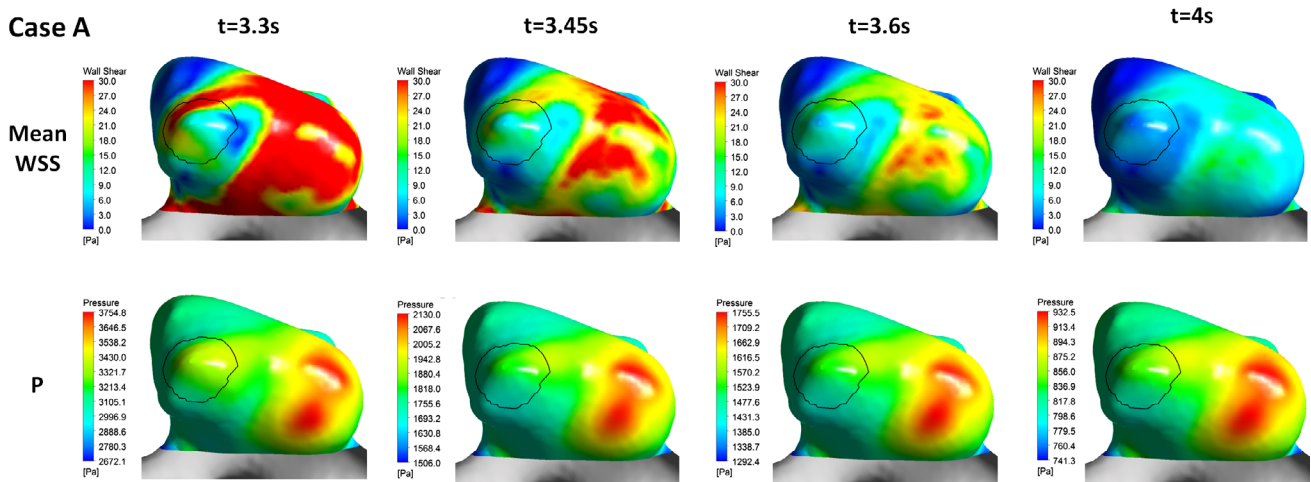

Fig. 9 Mean WSS and pressure on aneurysm at four cardiac cyclic phases ($t = 3.3$, 3.45, 3.6 and 4 s) in posterior artery flow rate

Table 5 shows the predicted MWSS of the complete aneurysm and rupture point areas at both the peak systole and the end diastole. Based on the present aneurysm locations (Table 1), the posterior artery flow rate was used at the vessel inlet, as shown in Fig. 5. In [13–15,25], lower WSS was deemed to correlate with aneurysm rupture, however that was based on the MWSS of the aneurysms. Here, at both phases, the present study further indicates that the MWSS at the rupture area is lower than the whole aneurysm, and this was also observed in [25]. In general, the reduction is more than 50 %, except in case A. If the 1 % rupture area is adopted, case A is around 77 % of the MWSS of the whole aneurysm.

Figure 7 shows the corresponding predicted MWSS on the aneurysm wall, where as expected lower level of WMSS is present near the rupture points. Further examination of the streamline patterns shown in Fig. 8 reveals the the complex recirculating vortices in the aneurysms. There are two branch type aneurysms (A and D) and three sidewall types (B, C and E). For the branch type aneurysm A, part of the inlet stream impacts near the rupture point, whereas in aneurysm D, impact point of the inlet stream is away from the rupture area. However, the inlet stream transports a higher level of momentum into the aneurysms, and hence higher levels of MWSS are predicted, as shown in Table 5. On the con-
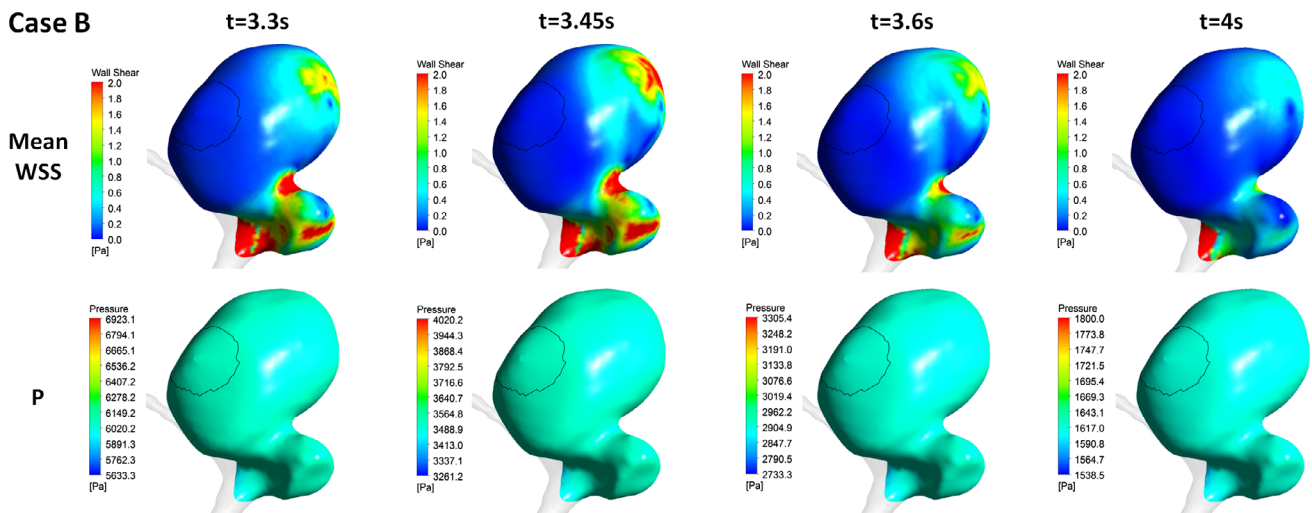
Fig. 10 Mean WSS and pressure on aneurysm at four cardiac cyclic phases (t = 3.3, 3.45, 3.6 and 4 s) in posterior artery flow rate-case B
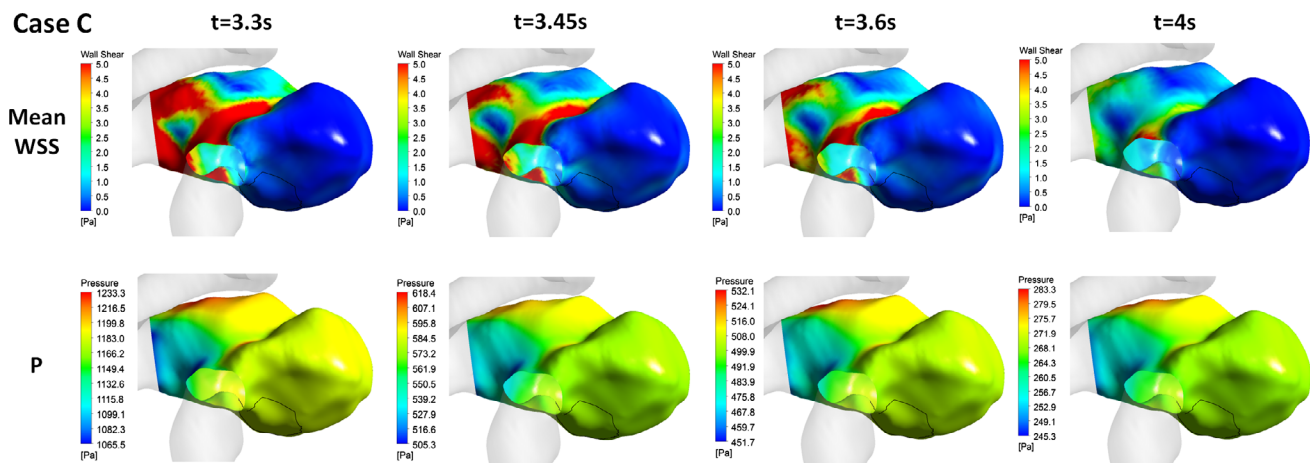

Fig. 11 Mean WSS and pressure on aneurysm at four cardiac cyclic phases (t = 3.3, 3.45, 3.6 and 4 s) in posterior artery flow rate-case C
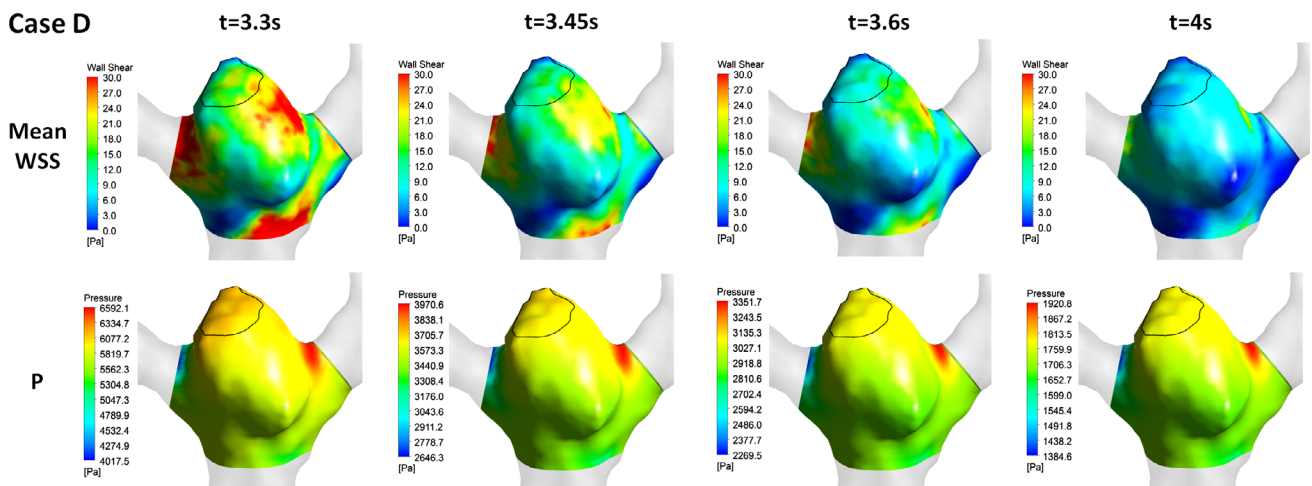

Fig. 12 Mean WSS and pressure on aneurysm at four cardiac cyclic phases (t = 3.3, 3.45, 3.6 and 4 s) in posterior artery flow rate-case D
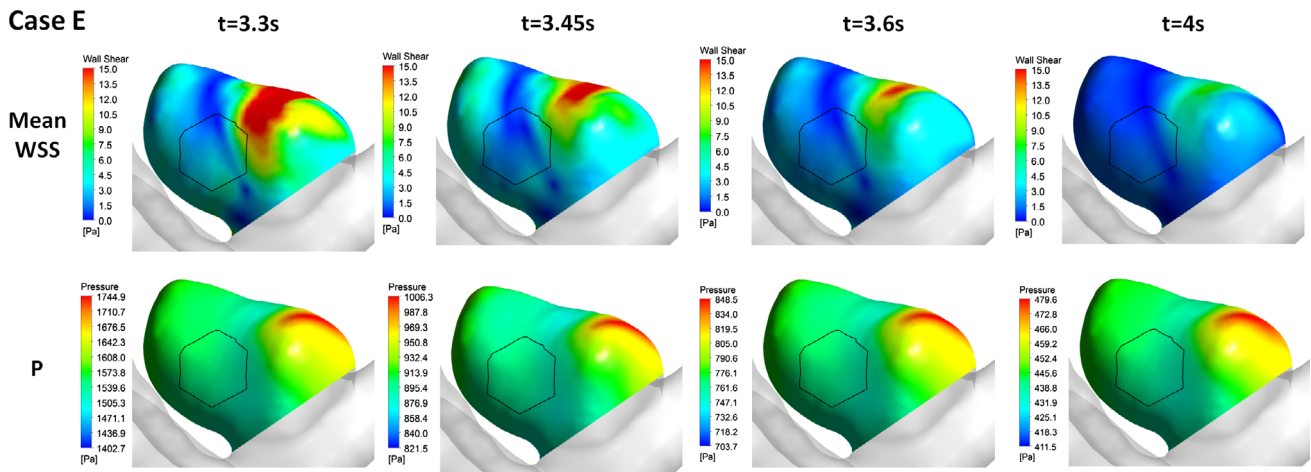
Fig. 13 Mean WSS and pressure on aneurysm at four cardiac cyclic phases (t = 3.3, 3.45, 3.6 and 4 s) in posterior artery flow rate-case E

Table 6 TAWSS and OSI predicted with posterior artery flow rates

Case	TAWSS (Pa)		OSI	
	Aneurysm wall	Rupture point	Aneurysm wall	Rupture point
A	9.39	9.18	0.0068	0.0030
B	0.76	0.04	0.0141	0.0107
C	1.25	0.33	0.0198	0.0175
D	22.61	8.21	0.0290	0.0045
E	3.58	1.97	0.0125	0.0129
Mean	7.518	3.946	0.0164	0.0097

trary, lower levels of MWSS are present for the sidewall type aneurysms.

Distributions of the aneurysm WSS and pressure at different phases of the cardiac cycle are shown in Figs. 9, 10, 11, 12, 13. As expected, lower WSS is present around the rupture area. For case A, the locally low WSS can be clearly observed near the rupture area, though the lowest WSS is located at other location. Also, the pressure rise due to the impact of the incoming stream can be seen from the pressure rise at the corresponding region.

It was shown in [13] that high OSI also correlates with rupture of the aneurysm and the threshold value was determined to be 0.0036. The present OSI is shown in Table 6, and the corresponding OSIs are as expected higher than the threshold value. However, the preset study also reveals that OSI at the rupture area is also lower than that in the whole aneurysm, except in case E, where it is marginally higher.

Influences of the inlet cardiac cycle are further examined by adopting higher flow rates from internal carotid artery and corresponding velocity profiles, as shown in Fig. 5. Simulated results are shown in Tables 7 and 8. Results using the cyclic velocity profiles are very similar to those adopting posterior artery flow rates, shown in Table 5. On the other

Table 7 MWSS at the rupture point and aneurysm wall with internal carotid artery flow rate

Case	Aneurysm wall (Pa)	Ruptured point (Pa)			Ruptured/aneurysm (%)		
		5 %	2.5 %	1 %	5 %	2.5 %	1 %
Peak systole (t = 3.3 s)							
A	76.12	70.81	75.67	64.52	93	99	85
B	2.44	0.19	0.17	0.16	8	7	7
C	6.01	1.17	1.02	0.78	19	17	13
D	175.89	59.37	44.85	44.86	34	25	26
E	27.96	6.45	4.12	3.33	23	15	12
End diastole (t = 4 s)							
A	15.587	11.63	10.06	6.74	75	65	43
B	1.098	0.12	0.10	0.08	11	9	8
C	1.934	0.52	0.39	0.28	27	20	15
D	67.432	20.68	16.15	15.65	31	24	23
E	8.971	2.42	1.71	1.45	27	19	16

Table 8 MWSS at the rupture point and aneurysm wall with internal carotid artery velocity conditions

Case	Aneurysm wall (Pa)	Ruptured point (Pa)			Ruptured/aneurysm (%)		
		5 %	2.5 %	1 %	5 %	2.5 %	1 %
Peak systole (t = 3.3 s)							
A	14.89	14.15	13.82	10.81	95	93	73
B	2.44	0.19	0.17	0.16	8	7	7
C	11.42	4.24	3.67	2.83	37	32	25
D	81.80	27.68	19.32	19.49	34	24	24
E	23.86	5.06	3.11	2.37	21	13	10
End diastole (t = 4 s)							
A	4.26	4.06	3.99	3.17	95	94	74
B	1.10	0.12	0.10	0.08	11	9	8
C	3.31	0.88	0.66	0.50	26	20	15
D	18.05	7.00	6.62	7.11	39	37	39
E	7.39	2.20	1.63	1.45	30	22	20

hand, applying the internal carotid artery flow rates at the inlet vessels generate a much higher influence on the branch type aneurysms, i.e. cases A and D, where the predicted WSS correlates strongly with the increase of inlet vessel velocity. As shown in Fig. 5 at the peak systole, the flow rate rise from ICA is about twice of that in PA. Thus, approximately four folds increase of the predicted WSS can be expected, and that is also reflected in Table 7 for cases A and D, except the peak systole phase for case D. However, the increase at the rupture region is not as extensive.

5 Conclusion

In the present study, the precise locations of contrast agent leakage of five ruptured cerebral artery aneurysms were successfully identified for the first time during CTA. Present morphological indices, namely the AR, UI and the non-spherical index confirm the previously proposed optimum thresholds for aneurysm rupture risk. Hemodynamic parameters, such as MWSS and OSI are further analyzed. It is demonstrated that the mean and time averaged wall shear stresses at rupture regions are lower than those over the surface of the aneurysms. Also, the levels of the OSI are higher than the reported threshold value, supporting the assertion that high OSI correlates with rupture of the aneurysm. However, the present results also show that OSI level at the rupture region is lower than that at the complete aneurysm. For side wall type aneurysms, different inlet flow rates have mild influences on the shear stresses distributions. On the other hand, for branch type aneurysms, the predicted wall shear stress correlates strongly with the increase of inlet vessel velocity. However, the increase at the rupture region is not as extensive. Since the present study adopts rigid wall, FSI

should be included in future study to study its influence. Also, immersed boundary method could be explored to assess its suitability to solve this flow [30,31].

References

1. Morita A, Fujiwara S, Hashi K, Ohtsu H, Kirino T (2005) Risk of rupture associated with intact cerebral aneurysms in the Japanese population: a systematic review of the literature from Japan. J Neurosurg 102:601–606
2. Wermer MJH, van der Schaaf IC, Algra A, Rinkel GJE (2007) Risk of rupture of unruptured intracranial aneurysms in relation to patient and aneurysm characteristics: an updated meta-analysis. Stroke 38:1404–1410
3. Wiebers DO, Whisnant JP, Huston J 3rd, Meissner I, Brown RD Jr, Piepgras DG, Forbes GS, Thielen K, Nichols D, O'Fallon WM, Peacock J, Jaeger L, Kassell NF, Kongable-Beckman GL, Torner JC (2003) International study of unruptured intracranial aneurysms investigators: unruptured intracranial aneurysms: natural history, clinical outcome, and risks of surgical and endovascular treatment. Lancet 362:103–110
4. Shiue I, Arima H, Hankey GJ, Anderson CS (2011) Location and size of ruptured intracranial aneurysm and serious clinical outcomes early after subarachnoid hemorrhage: a population-based study in Australia. Cerebrovasc Dis 31:573–579
5. Burleson AC, Turitto VT (1996) Identification of quantifiable hemodynamic factors in the assessment of cerebral aneurysm behavior on behalf of the subcommittee on biorheology of the scientific and standardization committee of the ISTH. Thromb Haemost 76:118–123
6. Dhar S, Tremmel M, Mocco J, Kim M, Yamamptp J, Siddiqui AH, Hopking LN (2008) Morphology parameters for intracranial aneurysm rupture risk assessment. Neurosurgery 63:185–196

7. Ma B, Harbaugh RE, Raghavan ML (2004) Three-dimensional geometrical characterization of cerebral aneurysms. Ann Biomed Eng 32:264–273

8. Shojima M, Oshima M, Takagi K, Torii R, Hayakawa M, Katada K, Morita A, Kirino T (2004) Magnitude and role of wall shear stress on cerebral aneurysm: computational fluid dynamic study of 20 middle cerebral artery aneurysms. Stroke 35:2500–2505

9. Cebral JR, Castro MA, Burgess JE, Pergolizzi RS, Sheridan MJ, Putman CM (2005) Characterization of cerebral aneurysms for assessing risk of rupture by using patient-specific computational hemodynamics models. AJNR Am J Neuroradiol 26:2550–2559

10. Liou TM, Li YC, Juan WC (2007) Numerical and experimental studies on pulsatile flow in aneurysmsarising laterally from a curved parent vessel at various angles. J Biomech 40:1268–1275

11. Boussel L, Rayz V, McCulloch C, Martin A, Acevedo-Bolton G, Lawton M, Higashida R, Smith WS, Young WL, Saloner D (2008) Aneurysm growth occurs at region of low wall shear stress: patient-specific correlation of hemodynamics and growth in a longitudinal study. Stroke 39:2997–3002

12. Cebral JR, Mut F, Weir J, Putman C (2011) Quantitative characterization of the hemodynamic environment in ruptured and unruptured brain aneurysms. AJNR Am J Neuroradiol 32:145–151

13. Xiang J, Natarajan SK, Tremmel M, Ma D, Mocco J, Hopkins LN, Siddiqui AH, Levy EI, Meng H (2011) Hemodynamic-morphologic discriminants for intracranial aneurysm rupture. Stroke 42:144–152

14. Shojima M, Oshima M, Takagi K, Torii R, Nagata K, Shirouzu I, Morita A, Kirino T (2005) Role of the bloodstream impacting force and the local pressure elevation in the rupture of cerebral aneurysms. Stroke 36:1933–1938

15. Jou LD, Lee DH, Morsi H, Mawad ME (2008) Wall shear stress on ruptured and unruptured intracranial aneurysms at the internal carotid artery. AJNR Am J Neuroradiol 29:1761–1767

16. Tezduyar TE, Sathe S, Cragin T, Nanna B, Conklin BS, Pausewang J, Schwaab M (2007) Modelling of fluid-structure interactions with the space-time finite elements: arterial fluid mechanics. Int J Numer Methods Fluids 54:901–922

17. Torii R, Oshima M, Kobayashi T, Takagi K, Tezduyar TE (2008) Fluid-structure interaction modeling of a patient-specific cerebral aneurysm: influence of structural modeling. Comput Mech 43:151–159

18. Valencial A, Ledermann D, Rivera R, Bravo E, Galvez M (2008) Blood flow dynamics and fluid-structure interaction in patient-specific bifurcating cerebral aneurysms. Int J Numer Methods Fluids 58:1081–1100

19. Torii R, Oshima M, Kobayashi T, Takagi K, Tezduyar TE (2009) Fluid-structure interaction modeling of blood flow and cerebral aneurysm: significance of artery and aneurysm shapes. Comput Methods Appl Mech Eng 198:3613–3621

20. Takizawa K, Moorman C, Wright S, Christopher J, Tezduyar TE (2010) Wall shear stress calculations in space time finite element computation of arterial fluid-structure interactions. Comput Mech 46:31–41

21. Takizawa K, Christopher J, Tezduyar TE, Sathe S (2010) Space-time finite element computation of arterial fluid-structure interaction with patient-specific data. Int J Numer Methods Biomed Eng 26:101–116

22. Torii R, Oshima M, Kobayashi T, Takagi K, Tezduyar TE (2011) Influencing factors in image-based fluid-structure interaction computation of cerebral aneurysms. Int J Numer Methods Fluids 65:324–340

23. Takizawa K, Schjodt K, Puntel A, Kostov N, Tezduyar TE (2012) Patient-specific computer modeling of blood flow in cerebral arteries with aneurysm and stent. Comput Mech 50:675–686

24. Takizawa K, Tezduyar TE (2014) Fluid-structure interaction modeling of patient-specific cerebral aneurysms. Visualization and Simulation of Complex Flows in Biomedical Engineering, Lecture Notes in Computational Vision and Biomechanics 12, doi:10.1007/978-94-007-7769-9-2

25. Omodaka S, Sugiyama S, Inoue T, Funamoto K, Fujimura M, Shimizu H, Hayase T, Takahashi A (2012) Local hemodynamics at the rupture point of cerebral aneurysms determined by computational fluid dynamics Analysis. Cerebrovasc Dis 34:121–129

26. Perktold K, Peter R, Resch M (1989) Pulsatile non-Newtonian blood flow simulation through a bifurcation with an aneurysm. Biorheology 26:1011–1030

27. Mantha AR, Benndorf G, Hernandz A, Metcalfe RW (2009) Stability of pulsatile blood flow at the ostium of cerebral aneurysms. J Biomech 42:1081–1087

28. Ford MD, Alperin N, Lee SH, Holdsworth DW, Steinman DA (2005) Characterization of volumetric flow rate waveforms in the normal internal carotid and vertebral arteries. Phys Meas 26:477–488

29. He XJ, Ku DN (1996) Pulsatile flow in the human left coronary artery bifurcation: average conditions. J Biomech Eng 118:74–82

30. Liao CC, Chang YW, Lin CA, McDonough JM (2010) Simulating flows with moving rigid boundary using immersed boundary method. Comput Fluids 39:152–167

31. Liao CC, Lin CA (2012) Simulations of natural and forced convection flows with moving embedded object using immersed boundary method. Comput Methods Appl Mech Eng 213:58–70